Numerical Exposure Assessment Report

SAR-NS_FCC-ISED-CE_6240351_WCM_V1.0

Customer: BURY GmbH & Co KG

Document Version 1.0 / 12th Sept, 2024

Author: David Schäfer

IMST GmbH
Carl-Friedrich-Gauß-Str. 2–4
47475 Kamp-Lintfort
Germany

Numerical Exposure Assessment Report

Versions[1]			
Release Date	**Nr.**	**Author**	**Comments**
12th Sept, 2024	1.0	David Schäfer	Initial version

Approval			
Name	**Job Title**	**Date**	**Signature**
David Schäfer	Preparation	12th Sept, 2024	
Jens Lerner	Review	12th Sept, 2024	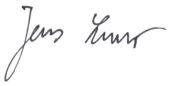

Laboratory	
Name and Address	IMST GmbH, Test Center Carl-Friedrich-Gauß-Str. 2–4 47475 Kamp-Lintfort
Accreditation	The Testcenter at IMST GmbH is a conformity assessment body (CAB) accredited by the German Accreditation Body "Deutsche Akkreditierungsstelle GmbH" (DAkkS), registered at D-PL-12139-01-00 and according to the accreditation scope D-PL-12139-01-02. It is a designated testing laboratory by the German Federal Network Agency for Electricity, Gas, Telecommunications, Post and Railway" Bundesnetzagentur" (BNetzA), registered at BNetzA-CAB-24/21-23.

Customer (Applicant / Manufacturer)		
Name and Address	BURY GmbH & Co KG Robert-Koch-Str. 1-7 32584 Löhne, Germany Contact: Johann Dshus	*Same as applicant*

Device Under Test (DUT)	
Type of DUT	Wireless Power Transfer Charger
Model Name	WCM
FCC ID	QZ9-WCM
ISED Cert. No.	5927A-WCM
Frequency Band	127.8 kHz
Active Elements	Three coils

[1] A new report revision replaces all previous versions, which hence become invalid.

Evaluation Results

Quantity inside flat phantom	Result*	Below exposure limit set by ...			
		ICNIRP	47 CFR § 1.1310	RSS-102 Issue 5 & 6	1999/519/EC
$SAR_{1g,\ max}$	48.2483 mW/kg	—**	Yes	Yes	—
$SAR_{10g,\ max}$	22.6785 mW/kg	Yes	Yes	Yes	Yes
$EIAV_{max}$	12.2591 V/m	Yes	—	Yes	—

*: Simulated values plus uncertainty penalties (if applicable, cf. section 3.2.5)

**: Not applicable combinations were indicated as "—"

Human Exposure Limits

Specific Absorption Rate (ICNIRP [1], 1999/519/EC [2])

Condition	Uncontrolled Environment (General Public)		Controlled Environment (Occupational)	
	SAR Limit	Mass Avg.	SAR Limit	Mass Avg.
SAR averaged over the whole body mass	0.08 W/kg	whole body	0.4 W/kg	whole body
Peak spatially-averaged SAR for the head, neck & trunk	2.0 W/kg	10 g of tissue*	10 W/kg	10 g of tissue*
Peak spatially-averaged SAR in the limbs/extremities	4.0 W/kg	10 g of tissue*	20 W/kg	10 g of tissue*
*: Defined as a tissue volume in the shape of a cube				

Specific Absorption Rate (RSS-102 Issue 5 [3], RSS-102 Issue 6 [4])

Condition	Uncontrolled Environment (General Public)		Controlled Environment (Occupational)	
	SAR Limit	Mass Avg.	SAR Limit	Mass Avg.
SAR averaged over the whole body mass	0.08 W/kg	whole body	0.4 W/kg	whole body
Peak spatially-averaged SAR for the head, neck & trunk	1.6 W/kg	1 g of tissue*	8 W/kg	1 g of tissue*
Peak spatially-averaged SAR in the limbs/extremities	4.0 W/kg	10 g of tissue*	20 W/kg	10 g of tissue*
*: Defined as a tissue volume in the shape of a cube				

Specific Absorption Rate (47 CFR Ch. I § 1.1310 [5])

Condition	Uncontrolled Environment (General Public)		Controlled Environment (Occupational)	
	SAR Limit	Mass Avg.	SAR Limit	Mass Avg.
SAR averaged over the whole body mass	0.08 W/kg	whole body	0.4 W/kg	whole body
Peak spatially-averaged SAR	1.6 W/kg	1 g of tissue*	8 W/kg	1 g of tissue*
Peak spatially-averaged SAR for extremities, such as hands, wrists, feet, ankles, and pinnae	4.0 W/kg	10 g of tissue*	20 W/kg	10 g of tissue*
*: Defined as a tissue volume in the shape of a cube				

Internal Electric Field (ICNIRP [1], RSS-102 Issue 5 [3], RSS-102 Issue 6 [4])

Condition	**Uncontrolled Environment** (General Public) **EIAV Limit**	**Controlled Environment** (Occupational) **EIAV Limit**
Peak EIAV @ f (in Hz)	$1.35 \cdot 10^{-4} \cdot f$ V/m	$2.7 \cdot 10^{-4} \cdot f$ V/m
Peak EIAV @ 127.7 kHz	17.2395 V/m	34.479 V/m

Frequency Scopes

Regulation	**SAR**		**EIAV**
	local	**whole body**	
ICNIRP	100 kHz – 6 GHz	100 kHz – 300 GHz	100 kHz – 10 MHz
47 CFR § 1.1310	100 kHz – 6 GHz		—*
RSS-102 Issue 5	100 kHz – 6 GHz		3 kHz – 10 MHz
RSS-102 Issue 6	100 kHz – 6 GHz		3 kHz – 10 MHz
1999/ 519/EC	100 kHz – 10 GHz		—
*: Not applicable combinations were indicated as "—"			

Contents

List of Figures

List of Tables

1 Introduction

1.1 Objective

The objective is the numerical exposure assessment of one Wireless Power Transfer (WPT) charger (further referred to as "device under test" or "DUT") designed by BURY GmbH & Co KG (further referred to as "customer"). In particular the Specific Absorption Rate (SAR, thermal hazard) and the internal electric field (EIAV[2], instantaneous nerve stimulation hazard) were investigated and compared to the exposure limits specified by ICNIRP [1], FCC [5], ISED [3, 4] and EUCO [2].

1.2 Simulation Method

All simulations were done with the Finite Difference Time Domain (FDTD) simulation tool Empire XPU [6]. A numerical model of the DUT was generated and validated by measurements of the magnetic field in its vicinity and measured inductance of the charging coil. The SAR and EIAV inside a flat phantom (human body part model) was investigated similar to the assessment procedures described in IEC/IEEE 62704-1 [7, 8]. The procedures were adapted to make them suitable for the low frequency of the DUT.

1.3 DUT Description

The 15 W, triple coil, wireless power charger "WCM" (further referred to as "device under test" or "DUT") can be used to charge portable devices like smart-phones (further referred to as "WPT receiver"). It is designed to be integrated into a vehicle, e.g. into the center console of a car. The DUT operates at a frequency of 127.8 kHz and features three charging coils. During operation only one of the three coils is excited/charging at a time. Which coil is used for charging is chosen by the DUT itself, depending on the placement of the WPT receiver device. Photos of the DUT are depicted in Figure 1 and a technical drawing including the DUTs dimensions is shown in Figure 2.

1.4 Setup for Reference Measurement

A validation of the numerical model was carried out by comparing the simulated magnetic field in the vicinity of the DUT with reference measurements.

Preliminary measurements showed that the worst-case configuration is given when the center coil is excited, so only this operation state was considered. The measurements were executed with a series production equivalent device, running in a testing operating mode at a fixed coil current of 3.42 A (RMS) at a frequency of 127.8 kHz. The customer pre-determined this to be the maximum expectable coil current during charging a WPT receiver. No WPT receiver was present during the reference measurements of the magnetic field.

The measurements were done on the behalf of the customer by the lab of "cetecom advanced GmbH" with the setup depicted in Figure 3. They used a SPEAG "DASY8" positioner system (cf.

[2] EIAV is the particular name of the post-processing/visualisation feature in Empire XPU. The averaging is optional and was disabled for this investigation.

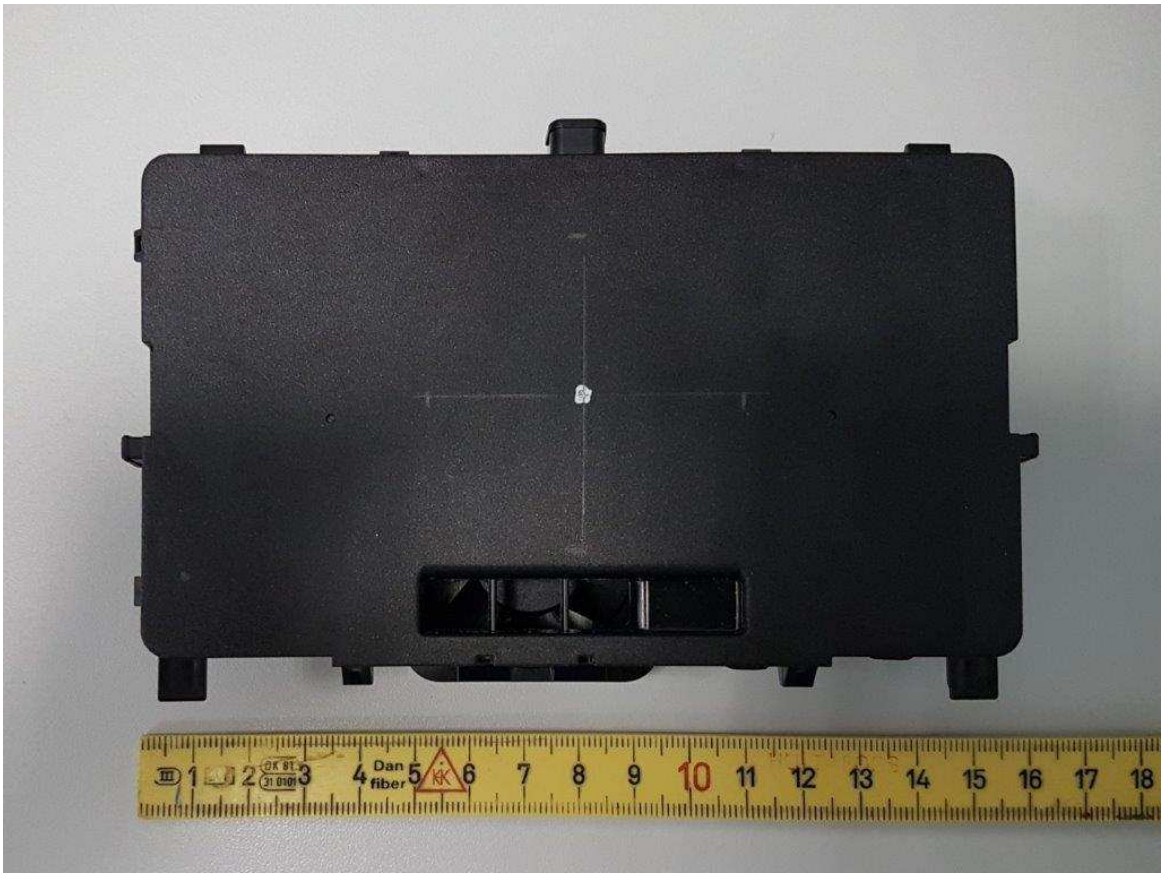

Figure 1: Photo of the DUT

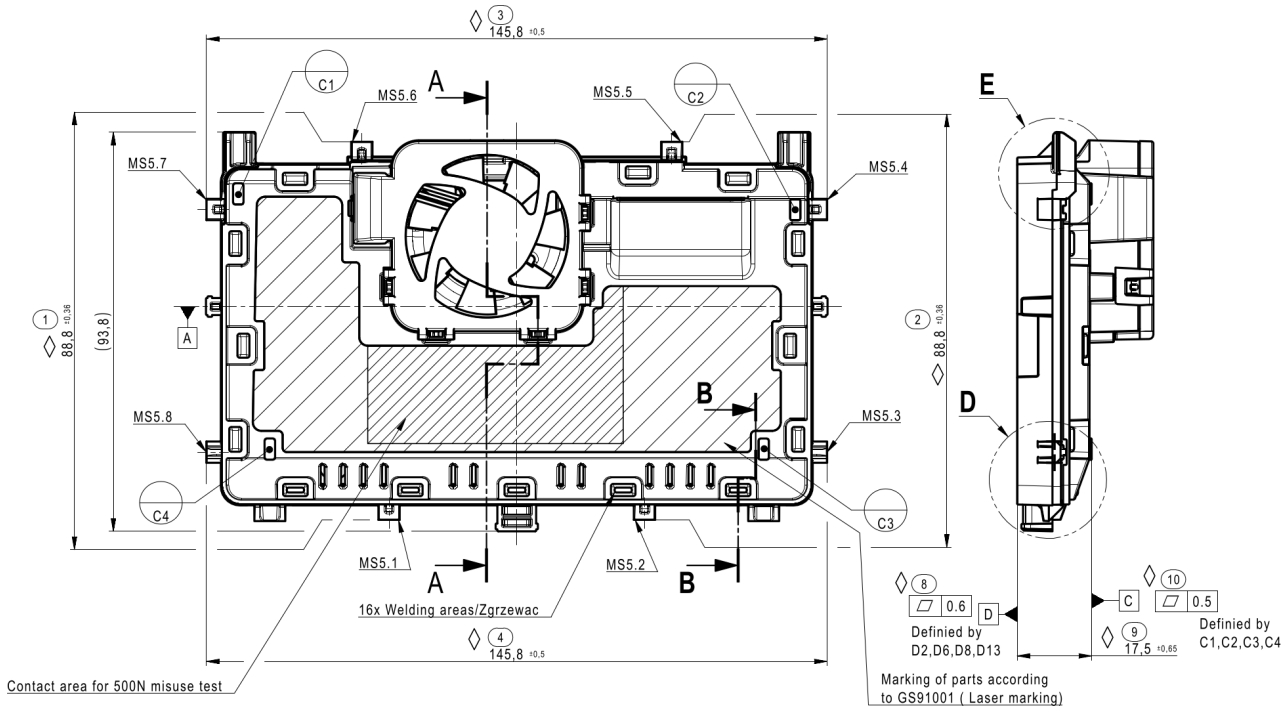

Figure 2: Technical drawing (excerpt) of the DUT provided by the customer, showing the DUTs dimensions in bottom and side view.

Figure 3a+c) and a "MAGPy-8H3D+E3D" field probe featuring "eight isotropic $1\,\mathrm{cm}^2$-H-field sensors, arranged at the corners of a 22 mm cube" (cf. Figure 3d). The first/lowest H-field sensor plane consisting of four H-field-sensors is located $7.5\,\mathrm{mm}$ from the probe tip. The field probe was positioned above the charging coil (cf. Figure 3b), and a line measurement was performed by lifting the probe upwards to different z-distances from the DUT whereby evaluating the magnetic field strength along the charging coil axis. Figures 3b and 3c show the lowest possible position of the field probe (touch position). The H-field values were used as reference measurements for the simulation, as provided in the measurement report named "1-7675-24-01-12_TR1-R01.pdf" from "2024-08-20" (Initial Release).

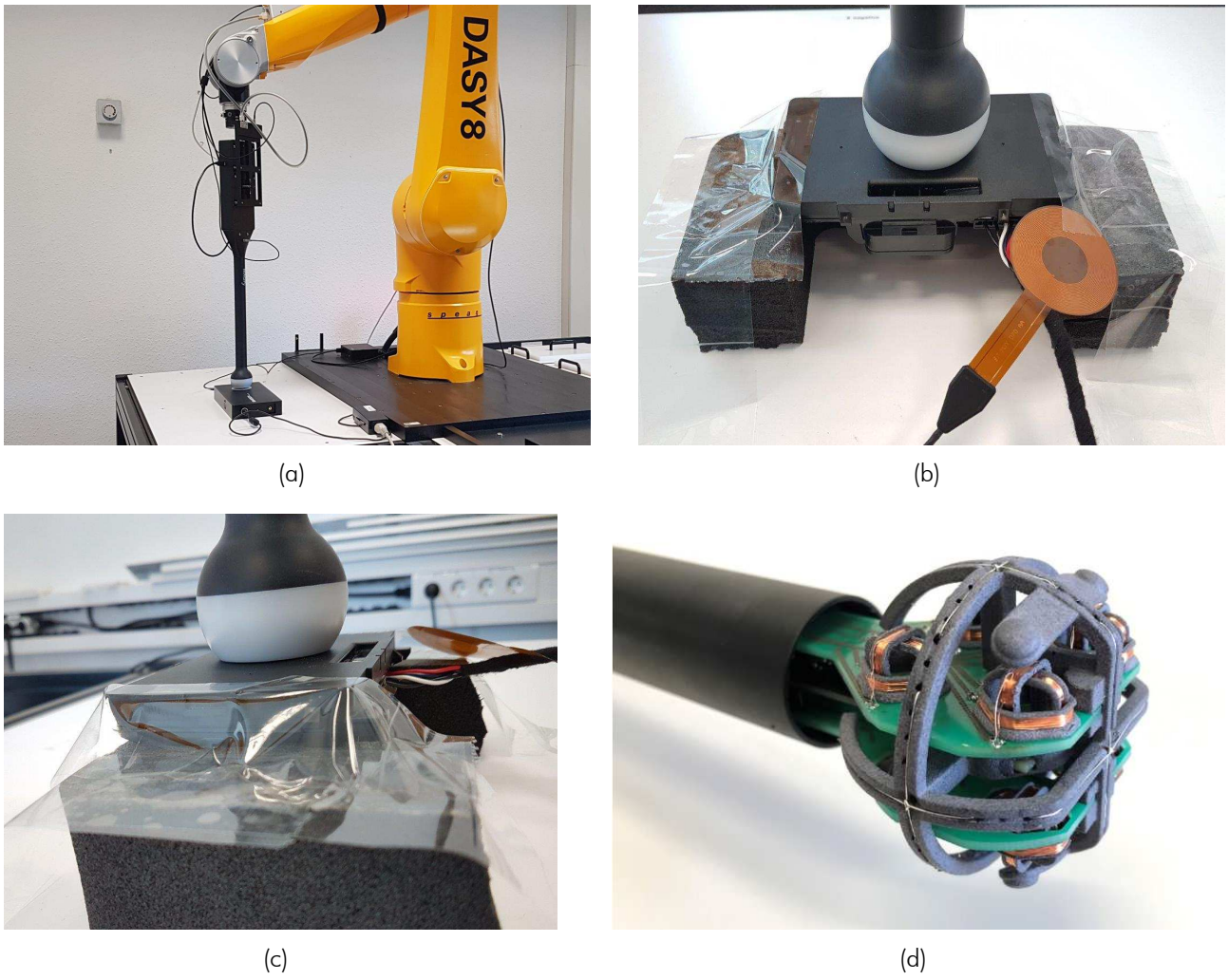

(a) (b)

(c) (d)

Figure 3: Measurement setup from the external lab of "cetecom advanced GmbH", showing (a) the SPEAG "DASY8" positioner with equipped "MAGPy-8H3D+E3D" probe, (b) and (c) the "MAGPy-8H3D+E3D" probe in touch position xy-centered over DUT coil and (d) a close-up of the "MAGPy-8H3D+E3D" probe insides. The depicted photos were taken from the measurement report and the measurement system manual.

2 EM Simulation Model

2.1 Model Setup

The simulation model of the DUT is based on STEP CAD data provided by the customer. The data was imported into Empire XPU and then rotated and moved so that the point of intersection between the middle charging coil axis and the DUTs top side is located in the origin of the coordinate system. Figure 4 shows a top and bottom 3D view of the simulation model.

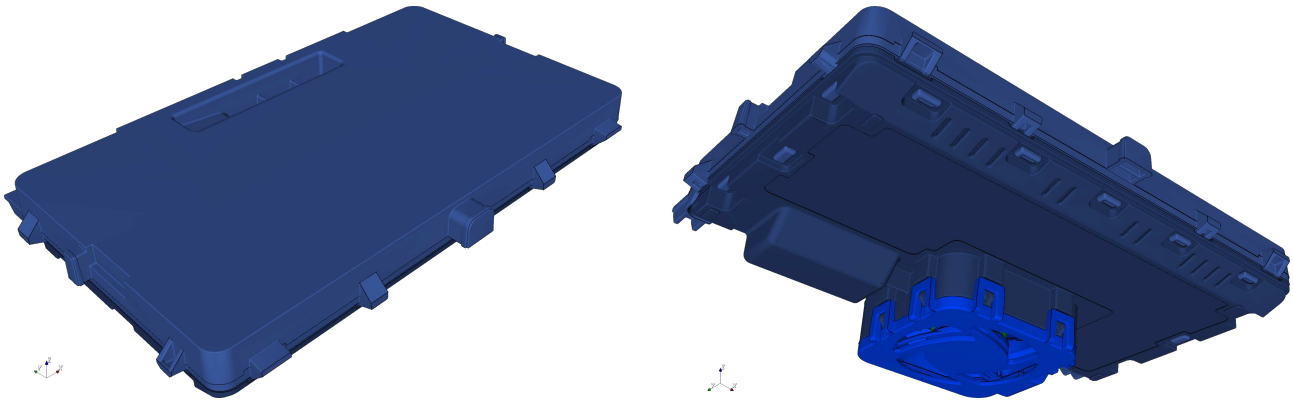

(a) (b)

Figure 4: Geometry of the Empire simulation model of the DUT, showing the outer view on the top (a) and bottom (b) side.

In Figure 5 the internal components are visible, including the three WPT charging coils. The center coil can be seen in red/orange, located in the middle and overlapping the two sideways coils. Its middle point is located at $x = y = 0\,\text{mm}$, $z = -3.140\,\text{mm}$ and the top side of the DUT housing is at $z = 0\,\text{mm}$.

Figure 6 shows an exploded view of the most important components of the simulation model. Based on the customers information the material properties were set as follows:

(a) Top housing (PC-ABS, $\epsilon_r = 3.0$)
(b) Top PCB (Copper traces, $\sigma = 57.14857 \cdot 10^6\,\text{S/m}$)
(c) Adhesive (Generic dielectric, $\epsilon_r = 2.25$)
(d) WPT coils (Copper, $\sigma = 56.18 \cdot 10^6\,\text{S/m}$)
(e) Ferrite ($\mu_r = 850$, $tan(\delta) = 0.0153$)
(f) Shielding (Aluminium, $\sigma = 35.00 \cdot 10^6\,\text{S/m}$)
(g) Adhesive (Generic dielectric, $\epsilon_r = 2.25$)
(h) Bottom PCB (Copper traces, $\sigma = 57.14857 \cdot 10^6\,\text{S/m}$)
(i) Bottom housing (PC-ABS, $\epsilon_r = 3.0$)
(j) Fan metal parts (PEC, $\sigma = inf\,\text{S/m}$) and dielectric parts (PBT, $\epsilon_r = 3.5$)

From the top PCB the graphite coating was removed from the simulation model, because it only has a small affect on the assessed quantities.

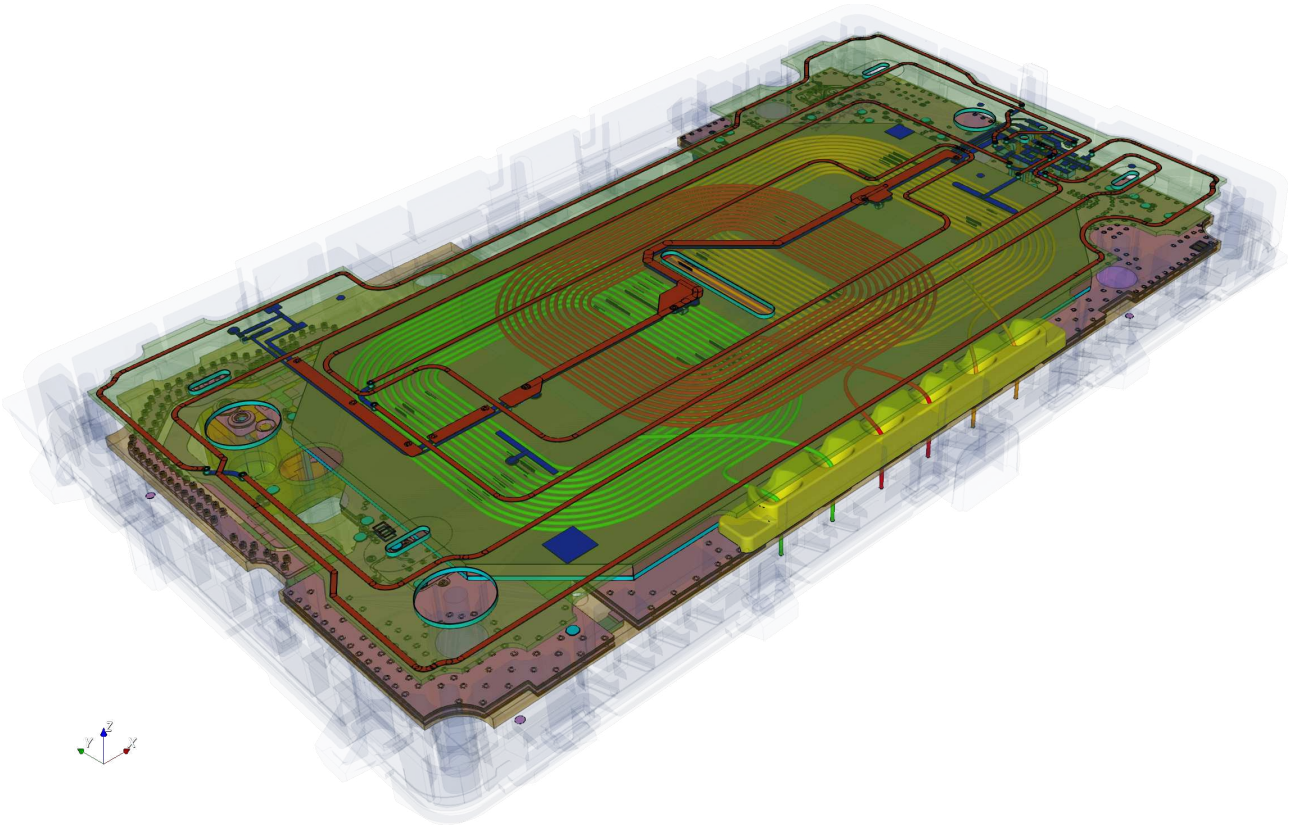

Figure 5: Geometry of the Empire simulation model of the DUT. The housing of the DUT is set transparent to show the internal components.

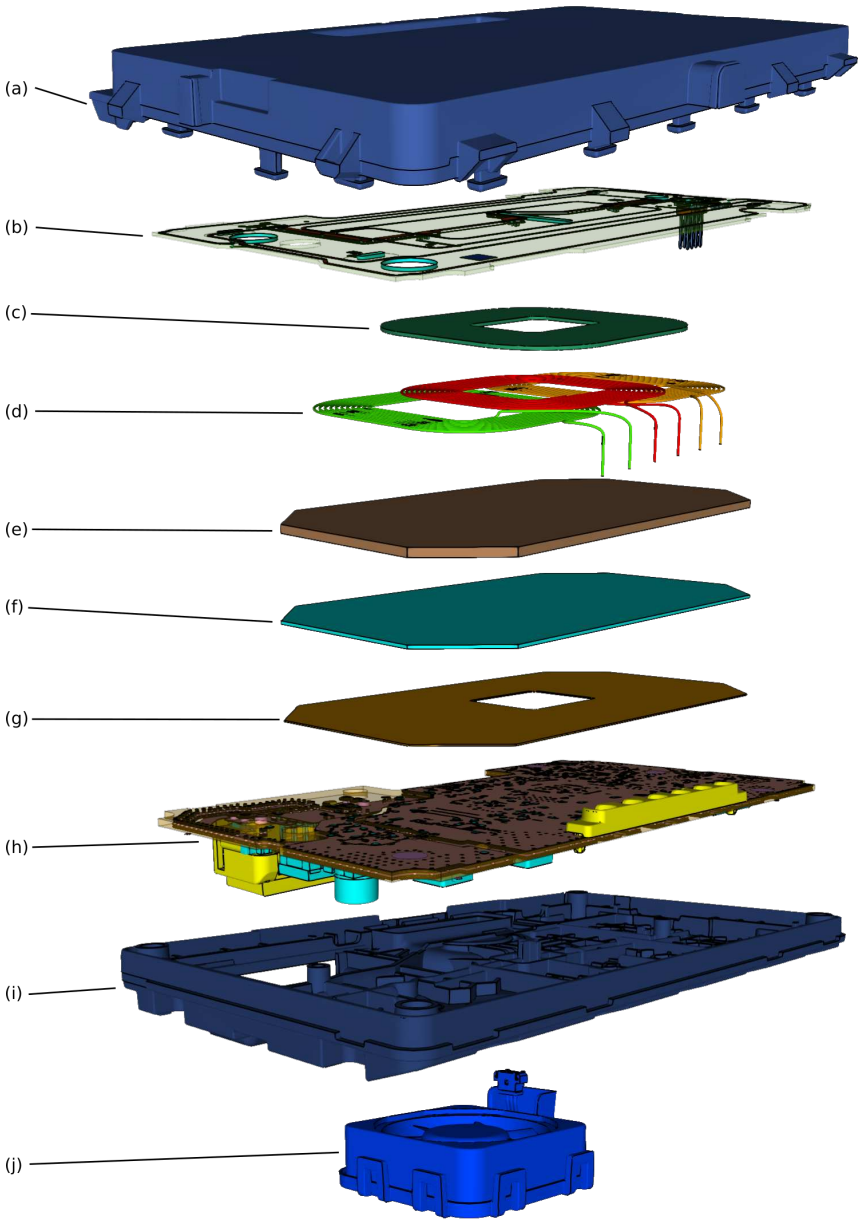

Figure 6: Geometry of the Empire simulation model of the DUT, showing an exploded view of the top housing (a), top PCB (b), adhesive (c), WPT coils (d), ferrite (e), shielding (f), adhesive (g), bottom PCB (h), bottom housing (i) and the fan module (j).

When the DUT is installed in a vehicle it is combined with an air grid, which encloses the DUTs housing as shown in Figure 7. The air grid allows air to pass by the bottom side of WPT receivers, cooling them during charging. Different variations of air grids can be combined with the DUT, depending on its mounting position inside the vehicle. The thinnest variant corresponding to the smallest possible separation distance was added to the numerical model and its material was set to TPS-SEBS ($\epsilon_r = 2.2$). The air grid was not present during the reference measurements, as can be seen from in Figure 3 in section 1.4.

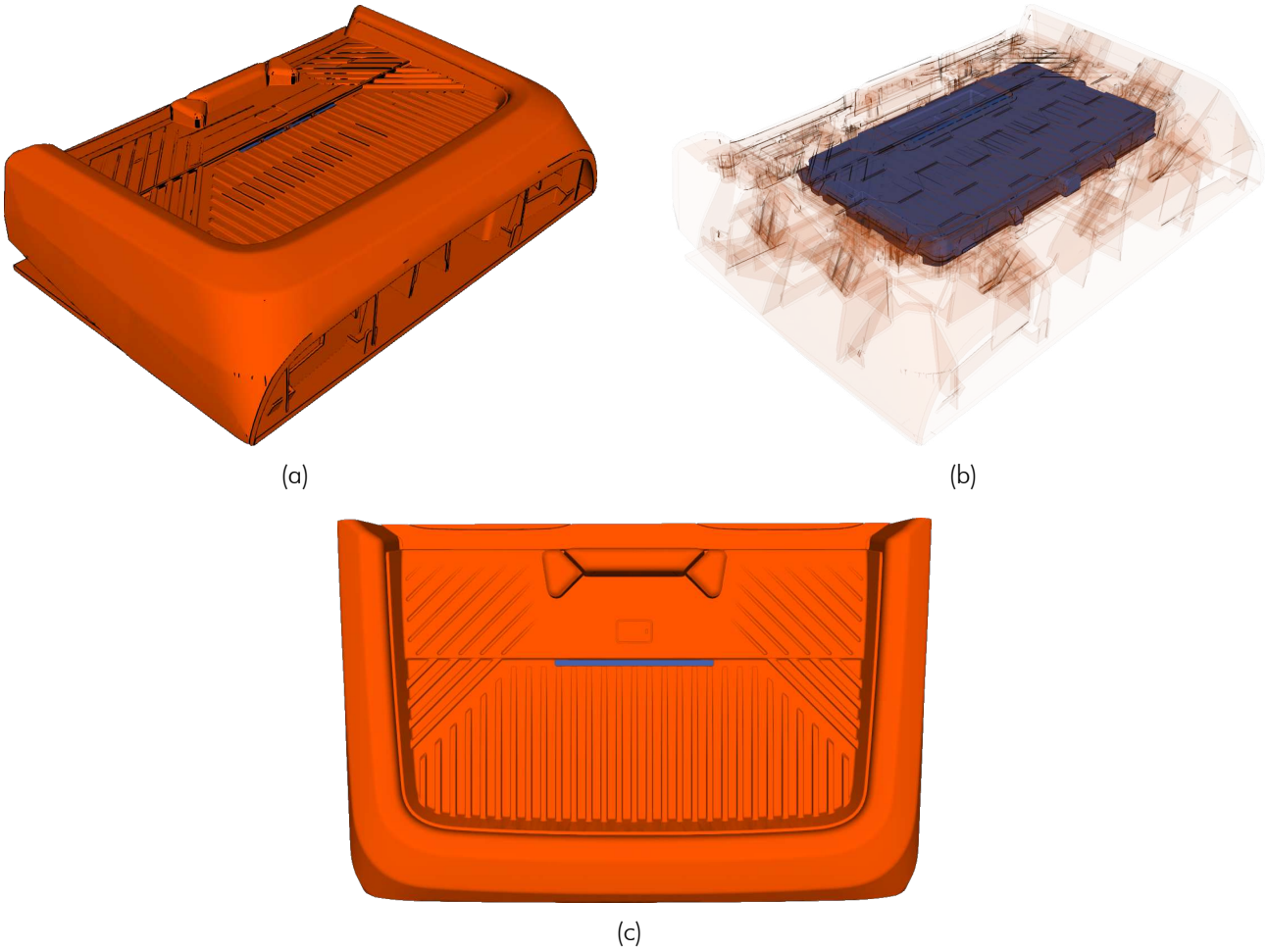

(a) (b)

(c)

Figure 7: Geometry of the air grid (rubber mat) which encloses the DUT.

2.2 Model Check

The simulation model was checked by comparing the simulated magnetic fields with the reference measurement (cf. section 1.4). During measurement and simulation the charging coil was excited with the maximum expectable current of $3.42\,\mathrm{A}$ (RMS) at a frequency of $127.8\,\mathrm{kHz}$. The simulation setup was unperturbed, meaning that it didn't include a WPT receiver device or phantom (human body model).

2.2.1 Magnetic Fields

Figure 8 shows a xz-cutplane for the simulated magnetic field strength through the center of the DUT. The colour legend is logarithmic with an 70 dB range. It can be seen how the main PCBs ground and the ferrite confine the main part of the magnetic field to the dedicated WPT receiver location above the DUT.

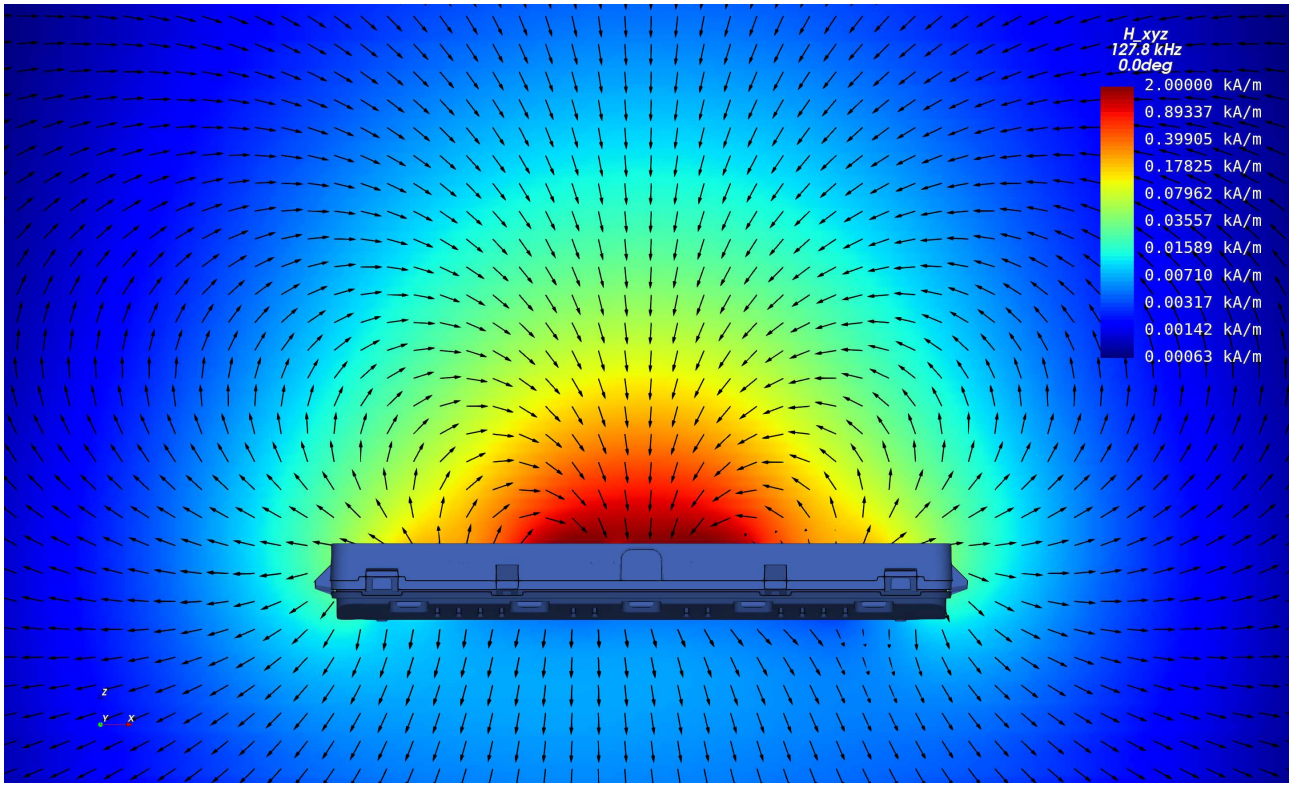

Figure 8: The simulated magnetic field displayed on a xz-plane through the DUT.

Analogue to the setup of the measurement (cf. section 1.4) the simulated magnetic field (H-field) strength was evaluated along the axis of the middle coil. The simulated line starts at $z = 0\,\mathrm{mm}$ which corresponds to the top of the DUTs housing. The measured line starts at $z = 8.0\,\mathrm{mm}$, so as close to the DUT as possible with respect to the necessary clearance and the "sensor center to tip distance" of the "MAGPy-8H3D+E3D" field probe (cf. section 1.4). As Table 1 and Figure 9 show, the simulated H-field is in agreement with the measurement.

z (mm)	Measurement (A/m)	Empire (A/m)
8.0	1081.230	1101.388
9.0	971.160	1014.581
10.0	888.060	933.803
11.0	830.080	859.302
12.0	772.720	791.077
13.0	715.360	727.410
14.0	658.000	668.613
15.0	600.650	614.687
16.0	543.300	566.881
17.0	495.350	521.332
18.0	461.000	478.040
19.0	431.410	442.737
20.0	401.830	408.703
21.0	372.240	375.937
22.0	342.660	348.257
23.0	313.070	322.265
24.0	285.530	297.961
25.0	265.530	275.787
26.0	249.890	255.697
27.0	234.250	237.689
28.0	218.620	220.906
29.0	202.980	205.317
30.0	187.350	190.920
31.0	171.720	178.288
32.0	160.000	166.129
33.0	151.290	154.444
34.0	142.880	144.902
35.0	134.480	135.657
36.0	126.070	126.709
37.0	117.670	118.886
38.0	109.270	111.533
39.0	102.050	104.652
40.0	96.570	98.235

Table 1: Tabular data of the measurement results shown in Figure 9 and the simulation results evaluated at the measurement locations up to a distance of 40.0 mm.

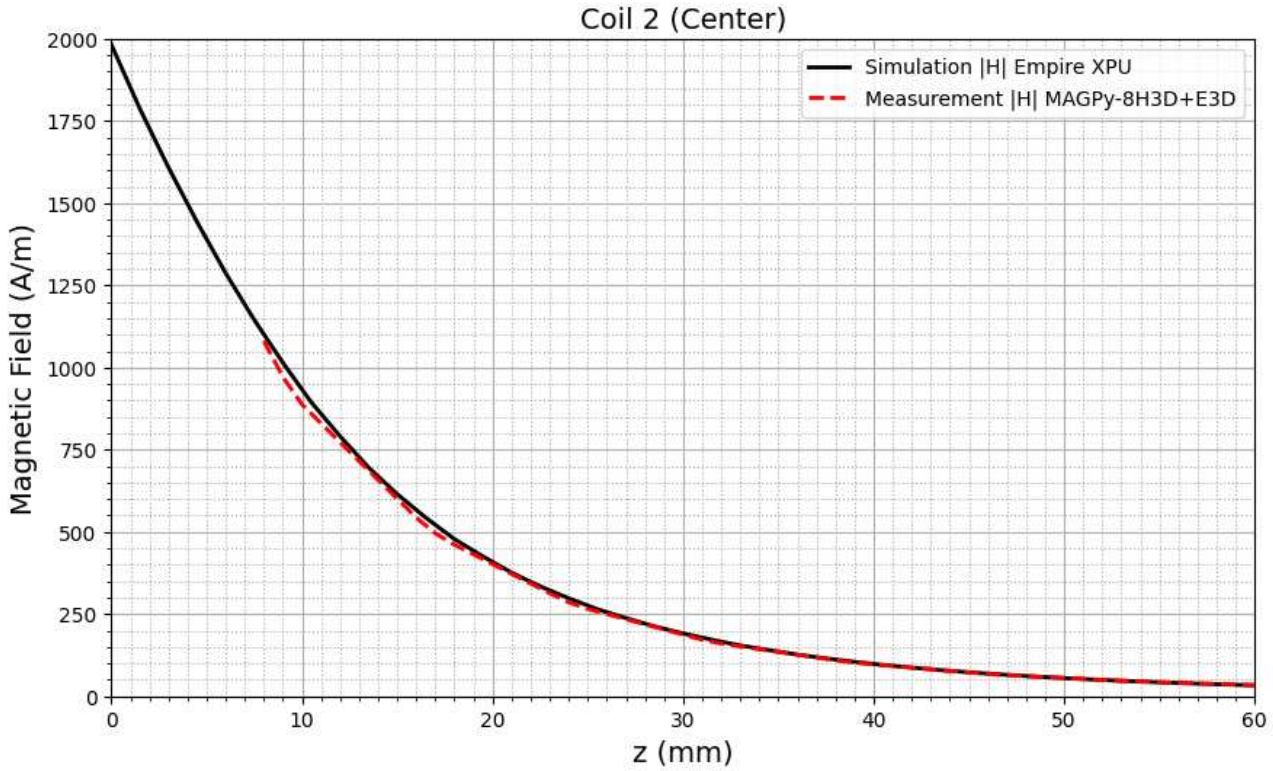

Figure 9: Curves for the line evaluation of the H-field (RMS values). The top of the DUTs dielectric housing is located at $z = 0\,\text{mm}$.

2.2.2 Coil Inductance

In addition to the magnetic fields also the inductance of the coil was used to check the simulation model. The measurement was done by the customer with the top part of the DUTs housing removed. With relative deviations of $-5.46\,\%$ (cf. Table 2) and $-6.23\,\%$ (cf. Table 3) the simulated inductance is in agreement with the value from the data sheet and the measurement.

	Data Sheet	Empire	Deviation
Coil Inductance	$11.300\,\mu\text{H} \pm 10\,\%$	$10.683\,\mu\text{H}$	$-5.46\,\%$

Table 2: Data sheet and simulated inductance.

	Measured	Empire	Deviation
Coil Inductance	$11.393\,\mu\text{H}$	$10.683\,\mu\text{H}$	$-6.23\,\%$

Table 3: Measured and simulated inductance.

2.2.3 Conclusion of Model Check

It can be concluded, that simulated magnetic field strength and inductance are in agreement (cf. Figure 9, Table 2 and Table 3) with the measurements from the external lab of "cetecom advanced GmbH" and the customer, indicating the accurate setup of the Empire simulation model.

3 SAR and EIAV Evaluation

For the evaluation of the Specific Absorption Rate (SAR) and the internal Electric field (EIAV) a box shaped flat phantom was added to the simulation model. The setup resembles the situation of someone touching the DUT just after a receiver removal which was in "charging mode" at maximum field. For the SAR evaluation the coil current could have been reduced according to the search mode duty cycle, but with respect to EIAV the continuous maximum expectable coil current was retained throughout the investigation.

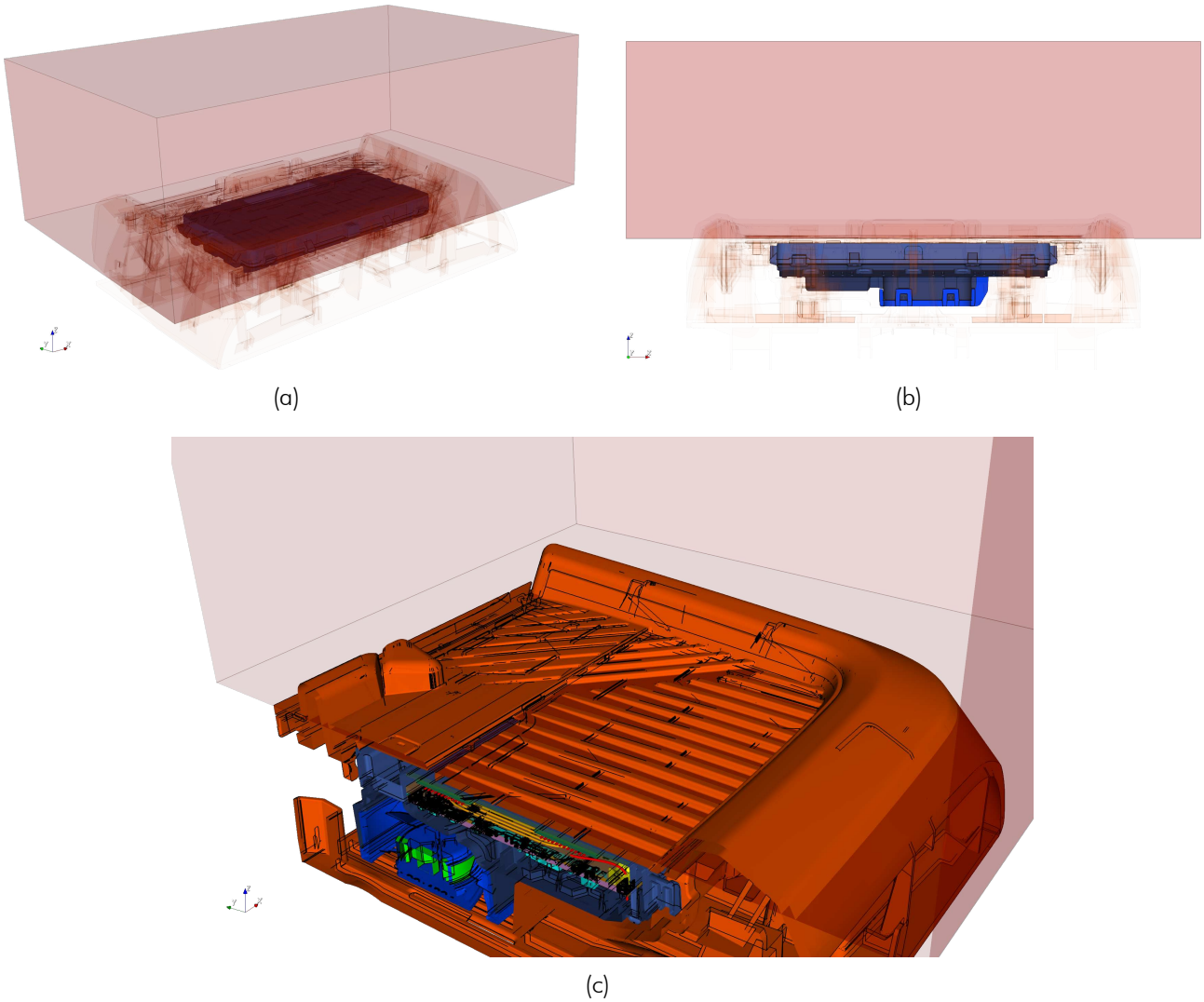

(a) (b)

(c)

Figure 10: Geometry of the flat phantom in 3D view (a) and side view (b). The phantom was brought down to touch position with the lowest reachable parts of the air grid (c).

The size of the phantom was larger than twice the outer dimensions of the DUT (without air grid). The phantom was centered (xy-direction) above the active charging coil at closest possible z—distance, virtually touching the lowest reachable parts of the air grid, i.e. the bottom of its crevices, as shown in Figure 10. This locates the phantoms bottom side (towards DUT) at $z = 2.475\,\text{mm}$. The phantoms material properties were set to the values given in RSS-102.NS.SIM [9] and IEC/IEEE 62209-1528 [10]. The following list concludes the most relevant phantom prop-

erties:

1. Geometric size: $d_x \cdot d_y \cdot d_z = 292\,\text{mm} \cdot 188\,\text{mm} \cdot 100\,\text{mm}$
2. Location of bottom side (towards DUT): $z = 2.475\,\text{mm}$
3. Relative permittivity: $\epsilon_r = 55$
4. Electrical conductivity: $\sigma = 0.75\,\text{S/m}$
5. Mass density: $\rho = 1000\,\text{kg/m}^3 = 1\,\text{g/cm}^3$

More details about the numerical model, like e.g. domain size, time step or total number of mesh cells, can be found in the appendix in section 4.1.

3.1 Simulation Results

Figure 11 and 12 show the simulated 1g- and 10g-averaged SAR and Figure 13 shows the simulated un-averaged EIAV. Table 4 lists the corresponding maximum values and their positions.

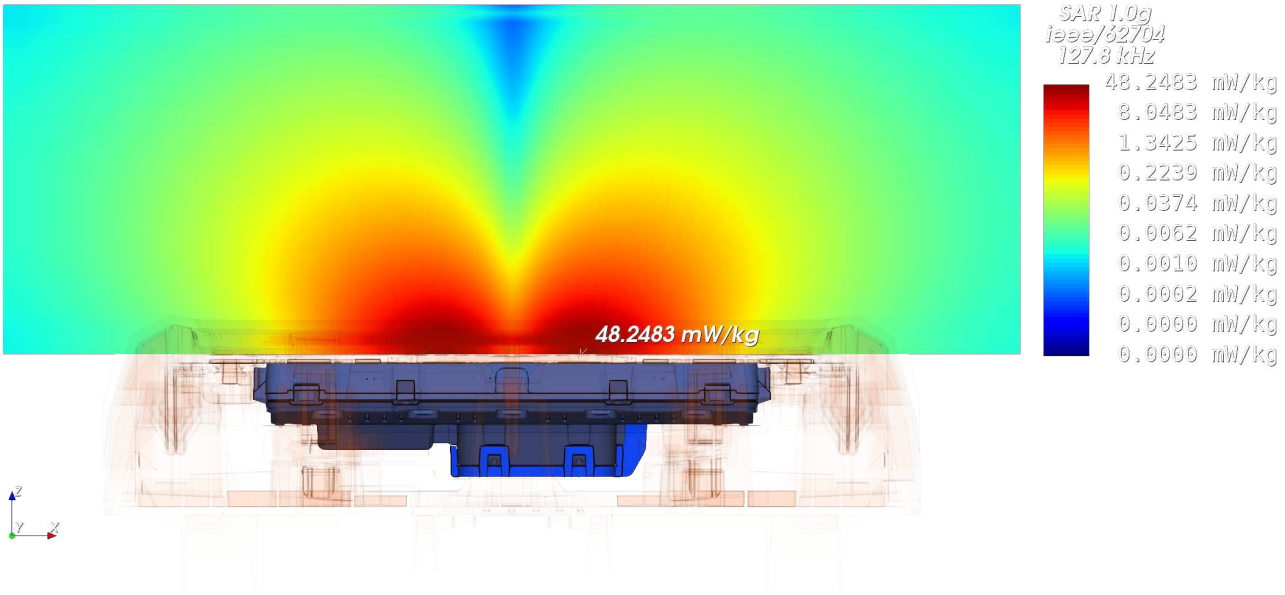

Figure 11: Cutplanes through the maxima of the simulated 1g-averaged SAR inside the flat phantom. The phantom geometry is not visible. The discontinuities at the phantom boundaries are caused by the averaging algorithm (cf. [7, Section 6.2.2]).

Quantity	Maximum Value	Position of Maximum x	y	z
$\text{SAR}_{1\text{g, max}}$	48.2483 mW/kg	19.550 mm	0.092 mm	2.600 mm
$\text{SAR}_{10\text{g, max}}$	22.6785 mW/kg	−19.850 mm	−0.509 mm	2.600 mm
$\text{EIAV}_{\text{unaveraged,max}}$	12.2591 V/m	18.950 mm	0.092 mm	2.600 mm

Table 4: SAR and EIAV maximum values with their corresponding positions.

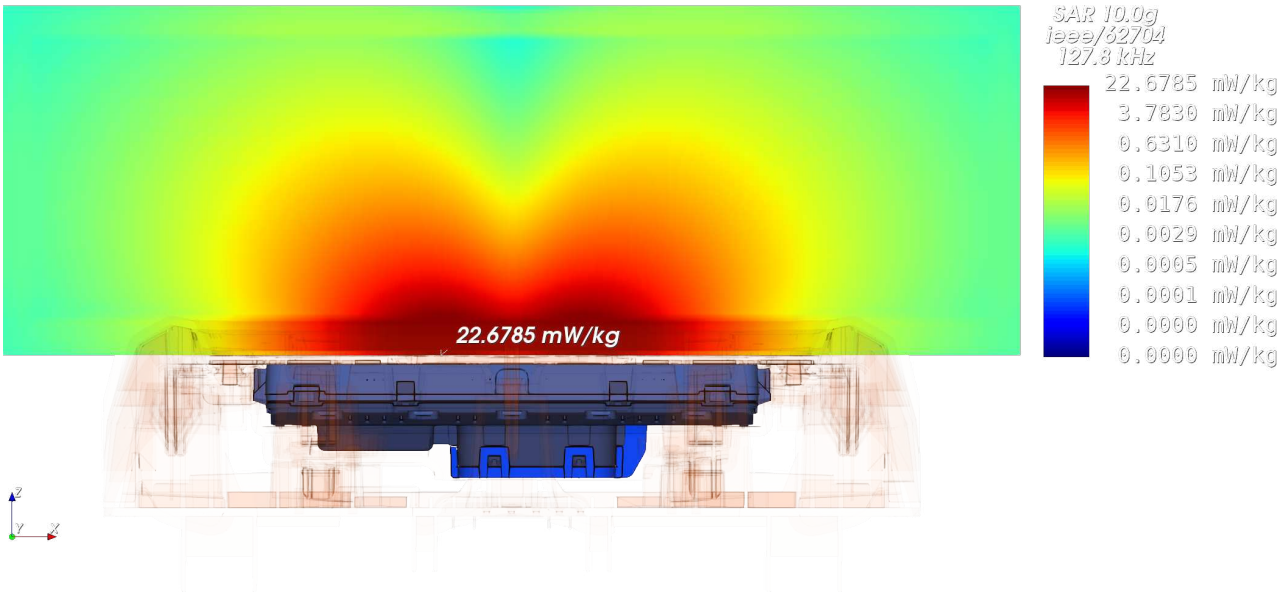

Figure 12: Cutplanes through the maxima of the simulated 10g-averaged SAR inside the flat phantom. The phantom geometry is not visible. The discontinuities at the phantom boundaries are caused by the averaging algorithm (cf. [7, Section 6.2.2]).

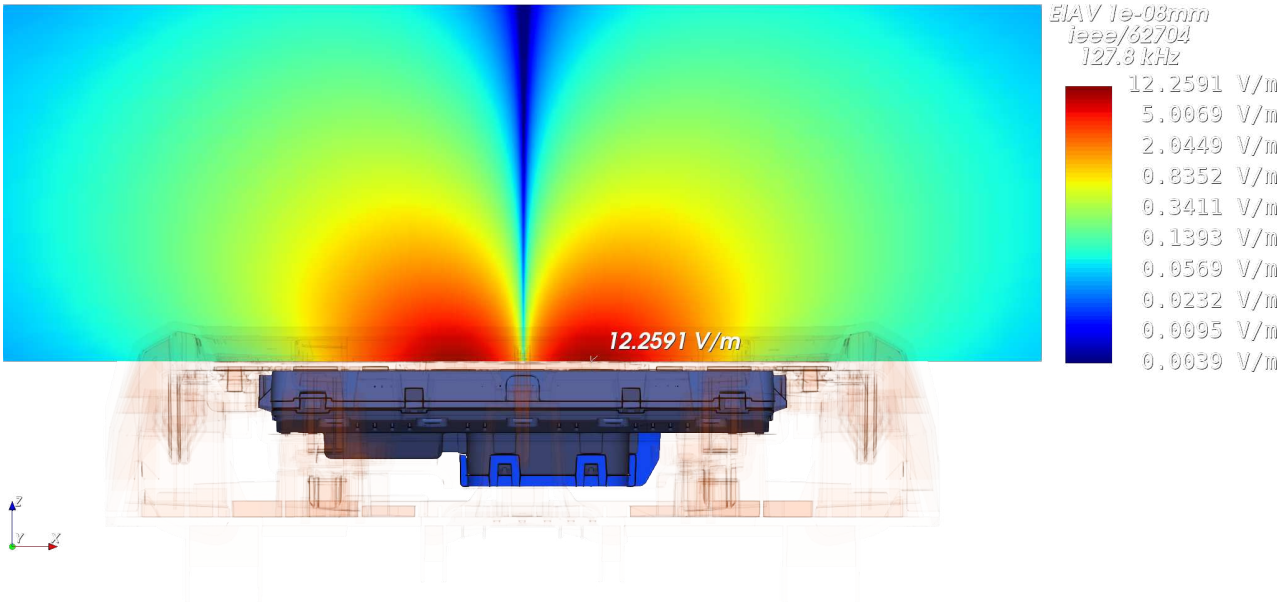

Figure 13: Cutplane through the maximum of the simulated EIAV inside the flat phantom. The phantom geometry is not visible.

3.2 Simulation Uncertainty

Based on chapter 7 of IEC/IEEE 62704-1 [7] the Combined- and Expanded Standard Uncertainty was calculated to analyse the accuracy of the results for the numerical model (further referred to as "reported model"). Because the DUTs operating frequency is below the scope of the standard, the procedure had to be modified. Details about this will be described in the following sections.

3.2.1 Simulation Parameter Related Uncertainty

The procedure for evaluating the simulation parameter related uncertainty (IEC/IEEE 62704-1 [7, section 7.2]) was modified as described in Table 5. Table 6, 7, 8 and 9 show the maximum SAR and EIAV for the investigated variants as well as their relative deviation from the reported model. Table 10, 11 and 12 show the budget of the SAR and EIAV uncertainty contributions of the simulation parameters.

Uncertainty Component	Applicability of the Procedure from IEC/IEEE 62704-1 [7, section 7.2]	Nr. of Variations
Positioning	Applicable. The distance between phantom and DUT was increased by +1 mesh step	1
Mesh Resolution	Not 1:1 applicable. Requested refinement is not practicable at 127.8 kHz. Instead, total number of mesh cells was increased by a factor of 2	1
Boundary Condition	Not 1:1 applicable, because $\lambda/4$ (=208 m) is way too large at 127.8 kHz. Instead, simulation domain was enlarged by 50% simultaneously in +/- x/y/z direction	1
Power Budget	Not applicable. No travelling wave conditions are given, so comparison with power absorbed in ABC is not possible. Excitation will be normalized to fixed port/coil current.	0
Convergence	Not 1:1 applicable. Instead it was simulated longer by a factor of (at least) 1.5 more time steps.	1
Phantom dielectrics	Not applicable / not indicated because fixed permittivity and conductivity from [9, 10] were used.	0

Table 5: Description of the modified procedure for obtaining the uncertainty budget.

3.2.2 Model Related Uncertainty

For distances $d < \lambda/2$ the IEC/IEEE 62704-1 [7, section 7.3.3] states that "*[...] the only way to determine the uncertainty of the DUT model is by SAR measurements*", which is not possible for the given frequency of the DUT. Therefore the procedure was modified by using the squared H-field values instead of SAR in [7, equation 14], similar to the assessment for distances $d \geq \lambda/2$ by [7, equation 13].

Phantom z-Position	2.475 mm	2.725 mm
$SAR_{1g,\,max}$	48.2483 mW/kg	46.1318 mW/kg
$SAR_{10g,\,max}$	22.6785 mW/kg	21.7766 mW/kg
$EIAV_{max}$	12.2591 V/m	11.9558 V/m
$SAR_{1g,\,max}$-Deviation	0 %	−4.39 %
$SAR_{10g,\,max}$-Deviation	0 %	−3.98 %
EIAV-Deviation	0 %	−2.47 %

Table 6: SAR and EIAV results for different phantom positions. The first data column corresponds to the reported model (cf. section 3.1).

Mesh Resolution	14.795 MCells	31.160 MCells
$SAR_{1g,\,max}$	48.2483 mW/kg	49.3564 mW/kg
$SAR_{10g,\,max}$	22.6785 mW/kg	23.0487 mW/kg
$EIAV_{max}$	12.2591 V/m	12.4850 V/m
$SAR_{1g,\,max}$-Deviation	0 %	2.30 %
$SAR_{10g,\,max}$-Deviation	0 %	1.63 %
EIAV-Deviation	0 %	1.84 %

Table 7: SAR and EIAV results for different mesh resolutions. The first data column corresponds to the reported model (cf. section 3.1).

Domain Size	492 mm · 388 mm · 415 mm	984 mm · 776 mm · 830 mm
$SAR_{1g,\,max}$	48.2483 mW/kg	48.2757 mW/kg
$SAR_{10g,\,max}$	22.6785 mW/kg	22.6912 mW/kg
$EIAV_{max}$	12.2591 V/m	12.2647 V/m
$SAR_{1g,\,max}$-Deviation	0 %	0.06 %
$SAR_{10g,\,max}$-Deviation	0 %	0.06 %
EIAV-Deviation	0 %	0.05 %

Table 8: SAR and EIAV results for different simulation domain sizes. The first data column corresponds to the reported model (cf. section 3.1). The domain was enlarged symmetrically in all spatial directions.

Time Steps	1.0 MSteps	2.0 MSteps
Energy Decay	−89.29 dB	−95.78 dB
$SAR_{1g,\ max}$	48.2483 mW/kg	49.2481 mW/kg
$SAR_{10g,\ max}$	22.6785 mW/kg	23.1352 mW/kg
$EIAV_{max}$	12.2591 V/m	12.3936 V/m
$SAR_{1g,\ max}$-Deviation	0 %	2.07 %
$SAR_{10g,\ max}$-Deviation	0 %	2.01 %
EIAV-Deviation	0 %	1.10 %

Table 9: SAR and EIAV results for different number of total time steps. The first data column corresponds to the reported model (cf. section 3.1).

Uncertainty Component	**Section in [7]**	**1g-SAR Tolerance in %**	**Probability Distribution**	**Divisor**	c_i	**1g-SAR Uncertainty in %**
Positioning	7.2.1	−4.39 %	R	1.73	1	−2.54 %
Mesh Resolution	7.2.2	2.30 %	N	1	1	2.30 %
Boundary Condition	7.2.3	0.06 %	N	1	1	0.06 %
Power Budget	7.2.4	*not appl.*	N	1	1	*not appl.*
Convergence	7.2.5	2.07 %	R	1.73	1	1.20 %
Phantom dielectrics	7.2.6	*not appl.*	R	1.73	1	*not appl.*
Combined Std. Uncertainty (k=1)						3.63 %

Table 10: Budget of the 1g-SAR uncertainty contributions of the simulation parameters, corresponding to IEC/IEEE 62704-1 [7, Table 3]. Note: N, R, U = normal, rectangular, U-shaped probability distributions.

Uncertainty Component	Section in [7]	10g-SAR Tolerance in %	Probability Distribution	Divisor	c_i	10g-SAR Uncertainty in %
Positioning	7.2.1	$-3.98\,\%$	R	1.73	1	$-2.30\,\%$
Mesh Resolution	7.2.2	$1.63\,\%$	N	1	1	$1.63\,\%$
Boundary Condition	7.2.3	$0.06\,\%$	N	1	1	$0.06\,\%$
Power Budget	7.2.4	*not appl.*	N	1	1	*not appl.*
Convergence	7.2.5	$2.01\,\%$	R	1.73	1	$1.16\,\%$
Phantom dielectrics	7.2.6	*not appl.*	R	1.73	1	*not appl.*
Combined Std. Uncertainty (k=1)						$3.05\,\%$

Table 11: Budget of the 10g-SAR uncertainty contributions of the simulation parameters, corresponding to IEC/IEEE 62704-1 [7, Table 3]. Note: N, R, U = normal, rectangular, U-shaped probability distributions.

Uncertainty Component	Section in [7]	EIAV Tolerance in %	Probability Distribution	Divisor	c_i	EIAV Uncertainty in %
Positioning	7.2.1	$-2.47\,\%$	R	1.73	1	$-1.43\,\%$
Mesh Resolution	7.2.2	$1.84\,\%$	N	1	1	$1.84\,\%$
Boundary Condition	7.2.3	$0.05\,\%$	N	1	1	$0.05\,\%$
Power Budget	7.2.4	*not appl.*	N	1	1	*not appl.*
Convergence	7.2.5	$1.10\,\%$	R	1.73	1	$0.63\,\%$
Phantom dielectrics	7.2.6	*not appl.*	R	1.73	1	*not appl.*
Combined Std. Uncertainty (k=1)						$2.42\,\%$

Table 12: Budget of the EIAV uncertainty contributions of the simulation parameters, analogue to the budget of the SAR uncertainty contributions of the simulation parameters to IEC/IEEE 62704-1 [7, Table 3]. Note: N, R, U = normal, rectangular, U-shaped probability distributions.

$$U_{\text{sim,model}} = max\left(\frac{|H^2_{\text{ref,n}} - H^2_{\text{sim,n}}|}{H^2_{\text{ref,max}}}\right) \tag{1}$$

$$= \left[\frac{|(971.16\,\text{A/m})^2 - (1014.58\,\text{A/m})^2|}{(1081.23\,\text{A/m})^2}\right]_{z=9.00\,\text{mm}} \tag{2}$$

$$= 7.38\,\% \tag{3}$$

Table 13 shows the budget of the uncertainty contributions of the model parameter. The customer stated an k=2 uncertainty of $1.33\,\text{dB} \Rightarrow 16.60\,\%$ for the measurements done by "cetecom advanced GmbH" (cf. section 1.4), so $8.30\,\%$ was used for the k=1 uncertainty of the measurement equipment and procedure.

Uncertainty Component (SAR)	Section in [7]	Tolerance in %	Probability Distribution	Divisor	c_i	Uncertainty in %
Uncertainty of the DUT model	7.3.2 or 7.3.3	$7.38\,\%$	N	1	1	$7.38\,\%$
Uncertainty of the phantom model	7.3.3	*not appl.*	N	1	1	*not appl.*
Uncertainty of the measurement equipment and procedure	-	$8.30\,\%$	N	1	1	$8.30\,\%$
Combined Std. Uncertainty (k=1)						$11.10\,\%$

Table 13: Budget of the uncertainty contributions of the model setup, corresponding to IEC/IEEE 62704-1 [7, Table 4]. Note: N, R, U = normal, rectangular, U-shaped probability distributions.

3.2.3 Model Validation

To validate the numerical model the equation 15 from IEC/IEEE 62704-1 [7, section 7.3.4] was calculated for the H-field line evaluation.

$$max\,(E_{\text{n}}) = max\left(\sqrt{\frac{(\nu_{\text{sim,n}} - \nu_{\text{ref,n}})^2}{(\nu_{\text{sim,n}} U_{\text{sim(k=2)}})^2 + (\nu_{\text{ref,n}} U_{\text{ref(k=2)}})^2}}\right) \tag{4}$$

$$= max\left(\sqrt{\frac{(H^2_{\text{sim,n}} - H^2_{\text{ref,n}})^2}{(H^2_{\text{sim,n}} U_{\text{sim(k=2)}})^2 + (H^2_{\text{ref,n}} U_{\text{ref(k=2)}})^2}}\right) \tag{5}$$

$$= \left[\sqrt{\frac{((521.33\,\text{A/m})^2 - (495.35\,\text{A/m})^2)^2}{((521.33\,\text{A/m})^2 \cdot (14.75\,\%))^2 + ((495.35\,\text{A/m})^2 \cdot (16.60\,\%))^2}}\right]_{z=17.00\,\text{mm}} \tag{6}$$

$$= 0.46 \leq 1 \tag{7}$$

Thereby $z = 17.00\,\text{mm}$ is the location "n" where the maximum value of E_n occurs. The condition/inequation is fulfilled, indicating that the deviation is within the expected uncertainty, and hence that the model is valid.

3.2.4 Uncertainty Budget

The budgets for simulation parameters related uncertainties and model related uncertainties were combined (k=1) and expanded (k=2) for 1g-SAR, 10g-SAR and EIAV as shown in table 14, 15 and 16 (see next page).

3.2.5 Uncertainty Penalty

The calculated Expanded Std. Uncertainties for SAR/EIAV do not exceed the maximum of $30\,\%$ stated in IEC/IEEE 62704-1 [7, Section 7.4]. Therefore uncertainty penalties as described in EN 62311 [11, Section 6.2, Equation 1] were not applied.

Uncertainty Component (1g-SAR)	Section in [7]	Tolerance in %	Probability Distribution	Divisor	c_i	Uncertainty in %
Uncertainty of the DUT model with respect to simulation parameters	7.2	3.63 %	N	1	1	3.63 %
Uncertainty of the developed numerical model of the DUT	7.3	11.10 %	N	1	1	11.10 %
Combined Std. Uncertainty (k=1)						11.68 %
Expanded Std. Uncertainty (k=2)						23.36 %

Table 14: Combined and expanded budget of the 1g-SAR uncertainty, corresponding to IEC/IEEE 62704-1 [7, Table 5]. Note: N, R, U = normal, rectangular, U-shaped probability distributions.

Uncertainty Component (10g-SAR)	Section in [7]	Tolerance in %	Probability Distribution	Divisor	c_i	Uncertainty in %
Uncertainty of the DUT model with respect to simulation parameters	7.2	3.05 %	N	1	1	3.05 %
Uncertainty of the developed numerical model of the DUT	7.3	11.10 %	N	1	1	11.10 %
Combined Std. Uncertainty (k=1)						11.52 %
Expanded Std. Uncertainty (k=2)						23.03 %

Table 15: Combined and expanded budget of the 10g-SAR uncertainty, corresponding to IEC/IEEE 62704-1 [7, Table 5]. Note: N, R, U = normal, rectangular, U-shaped probability distributions.

Uncertainty Component (EIAV)	Section in [7]	Tolerance in %	Probability Distribution	Divisor	c_i	Uncertainty in %
Uncertainty of the DUT model with respect to simulation parameters	7.2	2.42 %	N	1	1	2.42 %
Uncertainty of the developed numerical model of the DUT	7.3	11.10 %	N	1	1	11.10 %
Combined Std. Uncertainty (k=1)						11.36 %
Expanded Std. Uncertainty (k=2)						22.73 %

Table 16: Combined and expanded budget of the EIAV uncertainty, analogue to the budget of the SAR uncertainty from IEC/IEEE 62704-1 [7, Table 5]. Note: N, R, U = normal, rectangular, U-shaped probability distributions.

3.3 Additional Tests

3.3.1 Passive Receiver Impact

In the reported model the phantom is directly placed onto the air grid above the DUT. However, usually a WPT receiver such as a handset is placed on top of the DUT during charging operation. A receiver would increase the smallest possible approach distance, and its metal parts would act as a shield for the E- and H-fields, hence decreasing the exposure. To illustrate this effect, an additional simulation was done, whereby a passive phone receiver dummy was added to the model (cf. Figure 14).

Table 17 lists the maximum values for 1g-SAR, 10g-SAR and EIAV for the model with the passive receiver dummy. As expected they are noticeable lower than in case of the reported model. The before mentioned shielding effect also qualitatively changes the SAR/EIAV distribution, as can be seen in Figure 15.

Quantity	Reported Model	With Passive Receiver
$SAR_{1g,\,max}$	48.2483 mW/kg	0.0340 mW/kg
$SAR_{10g,\,max}$	22.6785 mW/kg	0.0184 mW/kg
$EIAV_{unaveraged,max}$	12.2591 V/m	0.3054 V/m

Table 17: SAR and EIAV maximum values for the model with the passive receiver dummy.

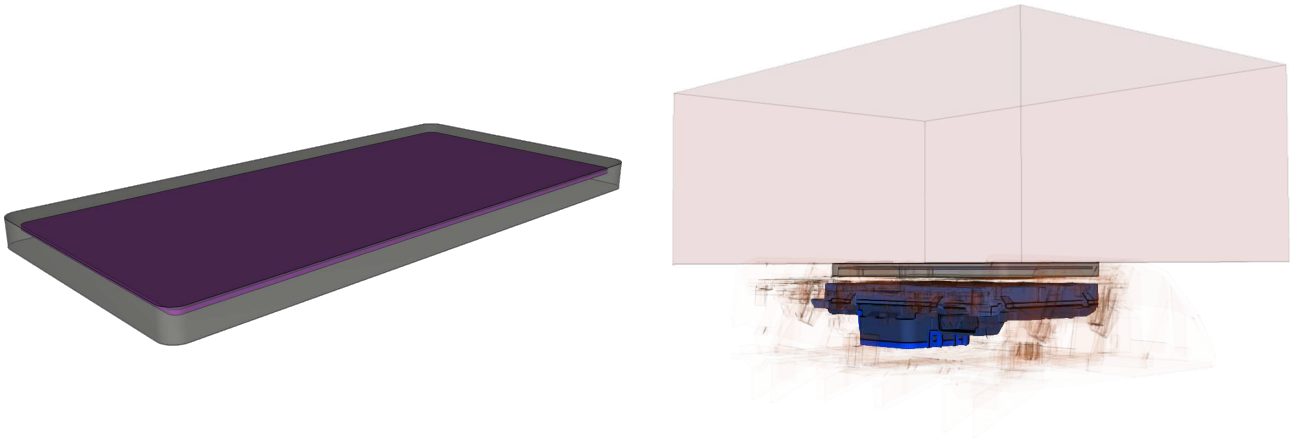

(a) (b)

Figure 14: Geometry of the passive receiver dummy, consisting of a $145 \cdot 70 \cdot 7$ mm dielectric housing with a metal plate inside (a). The receiver dummy was placed in between DUT and phantom (b).

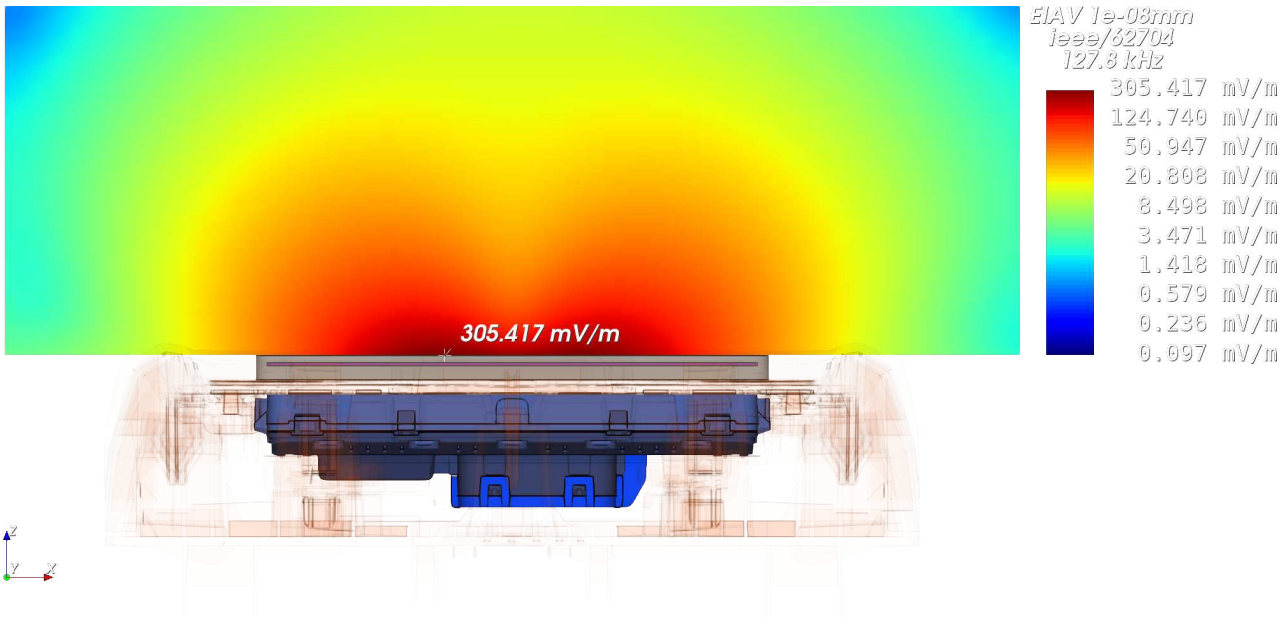

Figure 15: Cutplane through the maximum of the simulated EIAV inside the flat phantom for the model with the passive receiver dummy.

3.3.2 Field Behavior Across the Air-Phantom-Interface

Figure 16 depicts the behaviour of the E-field [3] and H-field across the air-phantom-interface ($z = 2.475\,\text{mm}$) of the reported model at the xy-location of the 1g-SAR maximum. The field behavior at the interface is as theoretically expected:

1. The tangential E-field components E_x and E_y are steady/continuous.
2. The normal E-field component E_z is discontinuous.
3. All H-field components are steady/continuous.
4. The H-field is practically unaffected (cf. Figure 16b vs. 17b) by the phantom, because of its low conductivity (cf. section 3).

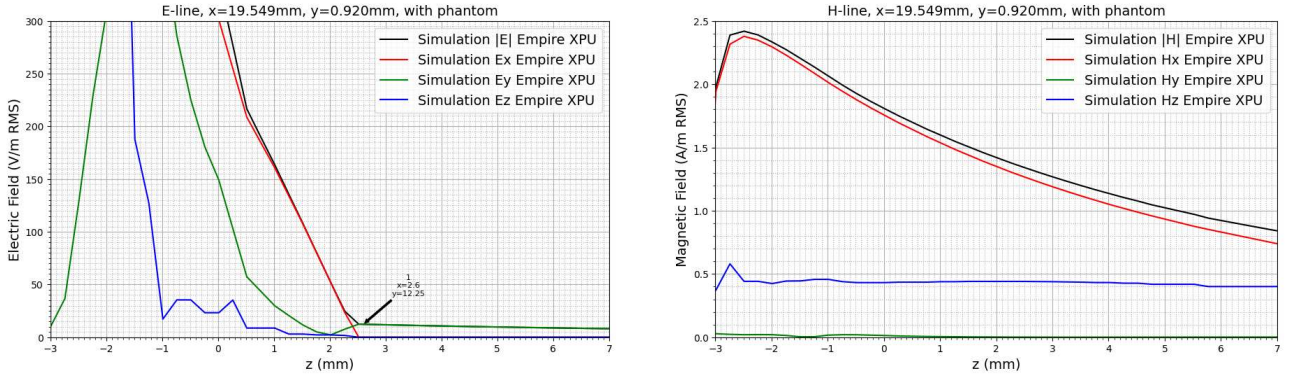

(a) (b)

Figure 16: Behavior of the E-field (a) and H-field (b) across the air-phantom-interface ($z = 0\,\text{mm}$) at the xy-location of the 1g-SAR maximum.

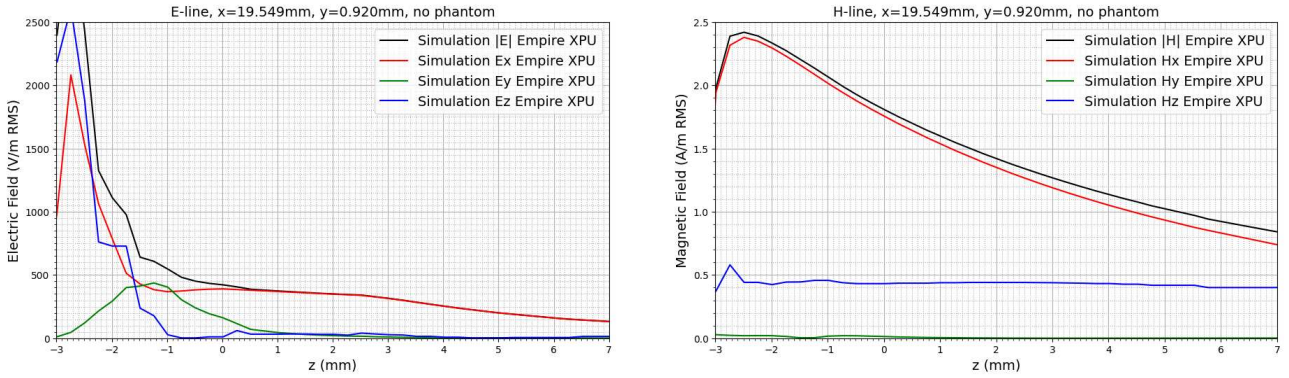

(a) (b)

Figure 17: E-field (a) and H-field (b) line plots analogue to Figure 16, but with no phantom present.

[3] It is very important to note that the simulated E-field distribution outside the phantom shown here only represents one possible physically correct distribution. Because the incident E-Field practically doesn't affect the exposure it was not validated and is hence presumably not the actual incident (!) E-Field distribution for the DUT.

3.3.3 Comparison Against Analytical Results

An additional check for the correctness of the numerical simulation results was done by replacing the large box shaped phantom (cf. section 3) with a small disc shaped phantom (cf. Figure 18). The disc has a height of 1 mm, a diameter of 6 mm and its axis equals the axis of the charging coil. The material properties of the disc phantom are the same as for the box shaped phantom.

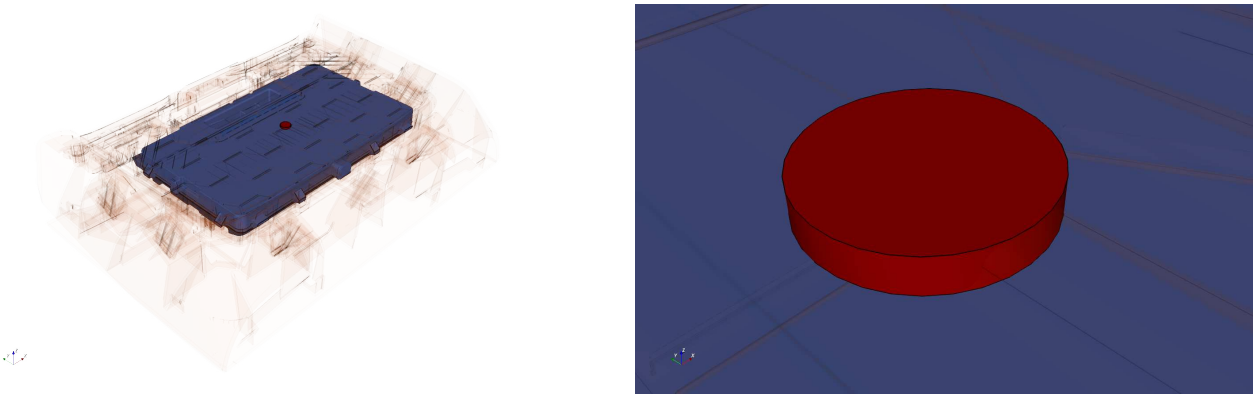

(a) (b)

Figure 18: Simulation geometry with the small disc shaped phantom.

Because the disc is small and its geometry is axial symmetric the internal E-field can be calculated analytically from the Maxwell-Faraday equation, considering the following conditions:

1. The H-field is approximately constant within the disc phantom: $\vec{H}(\vec{x}) = \vec{H}$
2. The H-field is oriented in z-direction within the disc phantom: $\vec{H}(\vec{x}) = H \cdot \vec{e}_\mathrm{z}$
3. The internal E-field is axial symmetric and oriented in azimuthal direction: $\vec{E}(\vec{x}) = E_\phi(r) \cdot \vec{e}_\phi$
4. The internal E-field has therefore no radial- and no z-component: $E_\mathrm{r} = E_\mathrm{z} = 0$

$$\oint_{\partial A} \vec{E}(\vec{x},t) \cdot \mathrm{d}\vec{s} = -\frac{\mathrm{d}}{\mathrm{d}t} \iint_A \vec{B}(\vec{x},t) \cdot \mathrm{d}\vec{A} \tag{8}$$

$$\Rightarrow 2\pi r E_\phi(r,t) = -\frac{\mathrm{d}}{\mathrm{d}t} \pi r^2 \mu_0 H_\mathrm{z} \cdot cos(\omega t) \tag{9}$$

$$\Leftrightarrow E_\phi(r,t) = -\frac{\mathrm{d}}{\mathrm{d}t} \frac{1}{2} r \mu_0 H_\mathrm{z} \cdot cos(\omega t) \tag{10}$$

$$= -\frac{1}{2} r \mu_0 H_\mathrm{z} \cdot \frac{\mathrm{d}}{\mathrm{d}t} \left(cos(\omega t)\right) \tag{11}$$

$$= -\frac{1}{2} r \mu_0 H_\mathrm{z} \cdot (\omega \cdot -sin(\omega t)) \tag{12}$$

$$= -\frac{1}{2} r \mu_0 H_\mathrm{z} \cdot (2\pi f \cdot -sin(\omega t)) \tag{13}$$

$$= r \mu_0 \pi f H_\mathrm{z} \cdot sin(\omega t) \tag{14}$$

$$= E_\phi(r) \cdot sin(\omega t) \tag{15}$$

$$\Rightarrow E_\phi(r) = r \mu_0 \pi f H_\mathrm{z} \tag{16}$$

Figure 19 shows the numerical simulation results of the internal E-field (EIAV) for the small disc phantom. The H-field within the disc phantom has values between $1537\,\mathrm{A/m}$ and $1629\,\mathrm{A/m}$.

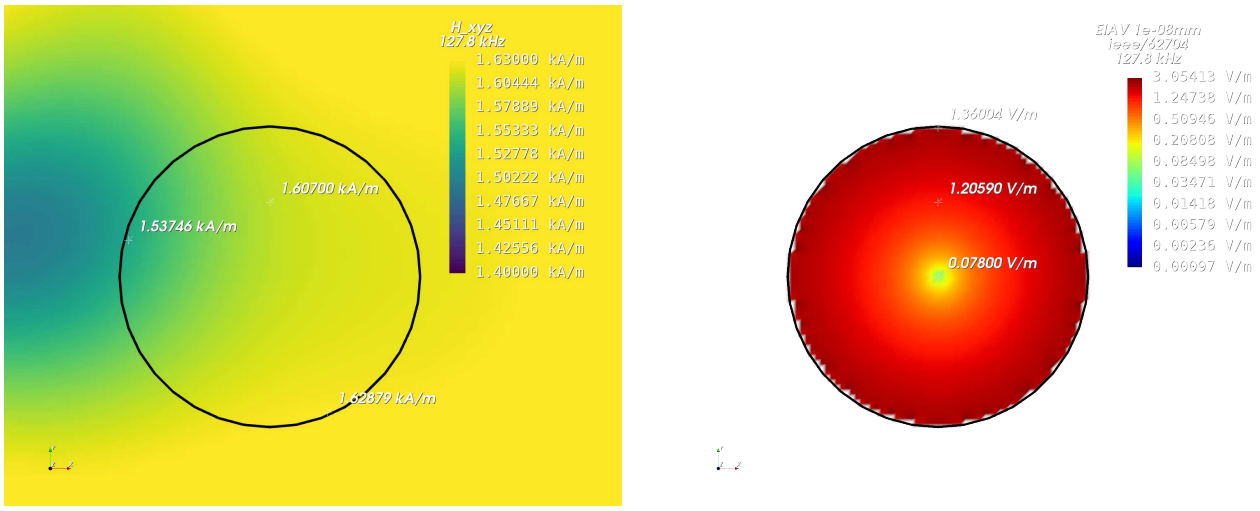

(a) (b)

Figure 19: H-field (a) and EIAV (b) within the small disc shaped phantom in the xy-plane.

At the position $x = 0\,\mathrm{mm}$ and $y = 1.5\,\mathrm{mm}$ the simulated H-field and EIAV within the disc phantom are:

$$H_{\mathrm{simul}}(r = y = 1.5\,\mathrm{mm}) = 1607\,\mathrm{A/m} \tag{17}$$
$$E_{\mathrm{simul}}(r = y = 1.5\,\mathrm{mm}) = 1.2059\,\mathrm{V/m} \tag{18}$$

The analytical internal E-field can be now calculated for the same position by inserting r, f and $H_z = H_{\mathrm{simul}}$ into equation (16):

$$E_{\mathrm{analytical}}(r = 1.5\,\mathrm{mm}) = E_{\phi,\mathrm{analytical}}(r = 1.5\,\mathrm{mm}) \tag{19}$$
$$= 1.5\,\mathrm{mm} \cdot \mu_0 \cdot \pi \cdot 127.8\,\mathrm{kHz} \cdot 1607\,\mathrm{A/m} \tag{20}$$
$$= 1.2162\,\mathrm{V/m} \tag{21}$$

The deviation of the simulation results from the analytical solution is therefore:

$$dev = \left| \frac{1.2059\,\mathrm{V/m} - 1.2162\,\mathrm{V/m}}{1.2162\,\mathrm{V/m}} \right| = 0.85\,\% \tag{22}$$

This demonstrates excellent agreement between simulation and analytical solution, considering the fact that the simulated H-field excited by the DUTs charging coil is not perfectly homogeneous within the disc phantom (cf. Figure 19a) as assumed for the analytical calculation. The comparison is supporting the results from the uncertainty analysis (cf. section 3.2) and the IEC/IEEE 62704-1 code verification [7, 8], indicating once again the accurate setup and simulation of the numerical DUT model.

3.4 Conclusion of the Evaluation

Summarizing the numerical exposure assessment of the DUT, the following can be stated:

1. The simulated magnetic field strength and the coil inductance are in agreement with the measurements (cf. section 2.2), indicating the accurate setup of the DUT simulation model (without phantom).
2. The investigated scenario (reported model) follows the worst-case assumption that:
   (a) The flat phantom is in direct contact with the DUT with no receiver in between.
   (b) The DUT is exciting its charging coil with the maximum expectable current, despite the fact that no receiver device is present.
   (c) The search mode duty cycle is neglected.
3. The model validation (cf. section 3.2.3) shows that in-equation 15 from IEC/IEEE 62704-1 is fulfilled, indicating a valid numerical model.
4. The uncertainty analysis returns Expanded Standard Uncertainties below the permissible 30% stated in IEC/IEEE 62704-1 section 7.4.
5. The evaluated maximum 1g-averaged SAR is $48.2483\,\mathrm{mW/kg}$.
6. The evaluated maximum 10g-averaged SAR is $22.6785\,\mathrm{mW/kg}$.
7. The evaluated maximum EIAV (internal Electric field, nerve stimulation hazard) is $12.2591\,\mathrm{V/m}$.
8. The following interpretation of the assessment results (decision rule) is carried out on the basis of ILAC-G8:09/2019, chap. 4.2.1 according to the "Simple Acceptance" decision rule - as far as this is not contradicted by other normative requirements.
9. With respect to the statements above, the conclusion of this numerical exposure assessment report is, that the DUT does not exceed the SAR and/or EIAV exposure limits specified by ICNIRP [1], FCC [5], ISED [3, 4] and EUCO [2]. A tabular evaluation can be found at the beginning of the report.

4 Appendix

4.1 Specific Information for Computational Modelling

FDTD algorithm implementation and validation: cf. [8]
Computing peak SAR from field components: cf. [8]
1g- and 10g-averaged SAR procedures: cf. [7, 8]
Processor type: AMD EPYC 7763 64-CORE PROCESSOR
Processor core usage: 32 cores
Memory usage: $969\,\mathrm{MB}$
Cell Size (min/max): $0.163\,\mathrm{mm}$ / $10.370\,\mathrm{mm}$
Domain Size: $492\,\mathrm{mm} \cdot 388\,\mathrm{mm} \cdot 415\,\mathrm{mm}$
Total amount of mesh cells: approx. $14.795\,\mathrm{MCells}$
Time step: $4.275560 \cdot 10^{-13}\,\mathrm{s}$
Total number of time steps: approx. $1.0\,\mathrm{MSteps}$
Simulation time: approx. 0hours and 14minutes and 5seconds
Simulation speed: $17222\,\mathrm{MCells/s}$
Excitation method: Gaussian pulse with $f_0 = 0\,\mathrm{Hz}$, $f_{\mathrm{BW}} = 50\,\mathrm{MHz}$
Phantom model implementation: cf. section 3
Tissue dielectric parameters: cf. section 3
Transmitter model implementation and validation: cf. section 2
Test device positioning: cf. section 3
Steady state termination procedures: A Gaussian pulse was used for the excitation and the simulation was terminated when the energy has dissipated to more than $-89.29\,\mathrm{dB}$.
Test results: cf. section 3

4.2 Abbreviations

Abbreviation	Description
CAD	Computer Aided Design
DUT	Device Under Test
EIAV	Averaged Internal Electric Field
EM	Electro Magnetic
FDTD	Finite Difference Time Domain
PCB	Printed Circuit Board
RF	Radio Frequency
RMS	Root Mean Square
SAR	Specific Absorption Rate
S/m	Siemens per meter $= 1/(\Omega m)$

4.3 Remarks

This report relates only to the item(s) evaluated. This report shall not be reproduced, except in its entirety, without the prior written approval of IMST GmbH. The results and statements contained in this report reflect the evaluation for the certain model described above. The manufacturer is responsible for ensuring that all production devices meet the intent of the requirements described in this report.

5 References

[1] International Commission on Non-Ionizing Radiation Protection (ICNIRP), "ICNIRP Guidelines for limitting Exposure to Electromagnetic Fields (100 KHz to 300 GHz)," 2020.

[2] European Council, "Council Recommendation of 12 July 1999 on the limitation of exposure of the general public to electromagnetic fields (0 Hz to 300 GHz), 1999/519/EC," July 1999.

[3] Innovation, Science and Economic Development Canada (ISED, Canada), "RSS-102 Issue 5 - Radio Frequency (RF) Exposure Compliance of Radiocommunication Apparatus (All Frequency Bands), with Amendment 1 from February 2, 2021," March 2015.

[4] ——, "RSS-102 Issue 6 - Radio Frequency (RF) Exposure Compliance of Radiocommunication Apparatus (All Frequency Bands)," December 2023.

[5] Federal Communications Commission (FCC, USA), "FCC Limits for Specific Absorption Rate (SAR), 47 C.F.R. § 2.1093, 10-1-20 Edition," 2020.

[6] IMST GmbH. (2023, September) Empire XPU, Version 8.2. Carl-Friedrich-Gauß-Str. 2-4, 47475 Kamp-Lintfort, Germany. [Online]. Available: http://empire.de

[7] IEC/IEEE 62704-1:2017, "IEC/IEEE International Standard – Determining the peak spatial-average specific absorption rate (SAR) in the human body from wireless communications devices, 30 MHz to 6 GHz - Part 1: General requirements for using the finite-difference time-domain (FDTD) method for SAR calculations," pp. 1–86, 2017.

[8] IMST GmbH, "Empire XPU - Code Verification Report for IEC/IEEE 62704-1, Version 8.2," February 2023.

[9] Innovation, Science and Economic Development Canada (ISED, Canada), "RSS-102.NS.SIM Issue 1 - Simulation Procedure for Assessing Nerve Stimulation (NS) Compliance in Accordance with RSS-102," December 2023.

[10] IEC/IEEE 62209-1528:2020, "IEC/IEEE International Standard - Measurement procedure for the assessment of specific absorption rate of human exposure to radio frequency fields from hand-held and body-mounted wireless communication devices – Part 1528: Human models, instrumentation, and procedures (Frequency range of 4 MHz to 10 GHz)," pp. 1–284, 2020.

[11] CENELEC, "Assessment of electronic and electrical equipment related to human exposure restrictions for electromagnetic fields (0 Hz to 300 GHz), EN IEC 62311," January 2020.